

VCNN-e: A vector-cloud neural network with equivariance for emulating Reynolds stress transport equations

Jiequn Han,^{1,*} Xu-Hui Zhou,^{2,*} and Heng Xiao^{2,†}

¹*Center for Computational Mathematics, Flatiron Institute, New York, NY 10010, USA*

²*Kevin T. Crofton Department of Aerospace and Ocean Engineering, Virginia Tech, Blacksburg, VA 24060, USA*

(Dated: January 5, 2022)

Developing robust constitutive models is fundamental and a longstanding problem for accelerating the simulation of complicated physics. Machine learning provides promising tools to construct constitutive models based on various calibration data. In this work, we propose a new approach to emulate constitutive tensor transport equations for tensorial quantities through a vector-cloud neural network with equivariance (VCNN-e). The VCNN-e respects all the invariance properties desired by constitutive models and faithfully reflects the region of influence in physics. By design, the model guarantees that the predicted tensor is invariant to the frame translation and ordering (permutation) of the neighboring points. Furthermore, it is equivariant to the frame rotation, i.e., the output tensor co-rotates with the coordinate frame. We demonstrate its performance on Reynolds stress transport equations, showing that the VCNN-e can effectively emulate the Reynolds stress transport model for Reynolds-averaged Navier–Stokes (RANS) equations. Such a priori evaluations of the proposed network pave the way for developing and calibrating robust and nonlocal, non-equilibrium closure models for the RANS equations.

I. INTRODUCTION

The first principle-based simulations of many practical problems arising from scientific and engineering applications are prohibitively expensive due to their multiscale nature. The constitutive relationship builds an effective bridge between different scales to mitigate this difficulty by simplifying and approximating the unresolved process at the microscopic scale with the resolved process in order to accelerate the simulations at the macroscopic scale. Taking industrial computational fluid dynamics (CFD) for instance, simulating the Reynolds averaged Navier–Stokes (RANS) equations for the mean flows fields are of ultimate interest in many engineering design tasks. To this end, constitutive models such as Reynolds stress models and eddy viscosity models are often introduced to describe unresolved turbulence and close the RANS equations. As such, they are also referred to as “closure models”, a term that is used interchangeably in this paper. Other examples include developing nonlinear stress-strain constitutive relationships to describe nonlinear elasticity and developing hydrodynamic models to approximate the motion of particles described by the kinetic equations or non-Newtonian fluids. Despite the enormous growth of available computational resources in the past decades, even to this day such closure models are still the backbone of practical engineering computations.

* Contributed equally

† Corresponding author. hengxiao@vt.edu

A. Invariance properties of constitutive models

In order to capture the essence of the physical phenomenon, the closure model should ideally express fundamental principles obeying physical constraints and meanwhile be as universally accurate as possible in the considered conditions. The traditional constitutive modeling usually relies on simple parametric models in combination with physical insight. However, as the number of involved state variables increases, it becomes more and more difficult to specify the form of the closure model and calibrate the parameters systematically, an essential obstacle known as the curse of dimensionality. The development of machine learning techniques in recent years, especially deep learning, has provided new tools to extract complicated relationships from massive data in an efficient and flexible way, thus a new possibility to data-driven constitutive modeling. In light of such strengths and promises, many machine learning-based constitutive models have been developed in the past few years in a wide range of application areas such as turbulence modeling [1–6] and computational mechanics [7–12] in general.

In some cases of physical modeling, it has been observed that machine learning-based models tend to achieve the best performance when it respects exactly the physical constraints and symmetries [13–17]. However, unlike the traditional constitutive modeling in which conventional wisdom can help restrict the set of admissible functions to obey physical constraints, such as frame independence [18–20], it is not straightforward to restrict flexible machine learning models like neural networks that take the raw state variables as input to be always genuinely physical. The challenge becomes more demanding when the constitutive relationship is nonlocal, i.e., the closure variable at location \mathbf{x}_i depends on the values of the resolved variables in a neighborhood region of \mathbf{x}_i rather than the value at \mathbf{x}_i solely. This situation is most evidently seen in turbulence models. The unresolved turbulent velocity fluctuation (which can be described by its second order statistics, i.e., the Reynolds stress) depends on an upstream neighborhood due to the convection and diffusion [21]. In such circumstances, an ideal closure model should be indifferent to the choice of material frame and the representation of resolved variables in the nonlocal region. In other words, the constitutive relationship should remain invariant when the coordinate system is translated or the index order of the discretized variable in the neighborhood permutes. Depending on the type of the closure variable, the constitutive relationship should also remain invariant or equivariant if the coordinate system is rotated. A recent work [22] considers specifically the rotational invariance/equivariance of a local relationship between a pair of tensors in the fluid dynamics. However, the technique developed there is insufficient to handle the nonlocal relationship. In a different vein, many recent works [see, e.g. 23–30] used machine learning models to approximate global operators or surrogate models defined by the PDEs, which also hold the promise to nonlocal constitutive modeling. However, the objectivity of these modeling approaches, such as frame-independence and permutational invariance mentioned above, has rarely been discussed. How to ensure that the machine learning models obey various physical constraints in the context of nonlocal constitutive modeling remains largely an open question.

B. Vector-cloud neural network with equivariance (VCNN-e)

One line of efforts to impose all the aforementioned symmetries in data-driven modeling is Deep Potential [31, 32] for interatomic potential and the vector-cloud neural network for nonlocal constitutive modeling [33]. At a high level, the original model consists of two modules, an embedding network and a fitting network. The former extracts

features that are translational, rotational, and permutational invariant from the raw input, and the latter predicts the output with the desired symmetry. This work focuses on generalizing the vector-cloud neural network (VCNN) [33] to develop a nonlocal closure model for *tensorial* output quantities. Compared to VCNN, in which the closure variable is a rotational invariant scalar [33], the main innovation of the present work is to tackle the closure problem in which the closure variable is a rotational equivariant tensor. To this end, we adopt the idea of Sommers et al. [34] to equip the VCNN with equivariance for tensorial outputs while preserving its general approximation ability. Furthermore, we extend the VCNN equipped with equivalence to correctly represent the function space that is uniquely required for turbulence modeling. In so doing, we obtain a vector-cloud neural network with equivariance (VCNN-e) that satisfies all the symmetries and function space requirements for the modeling of Reynolds stresses. To demonstrate the merits of the proposed VCNN-e framework, we test it for emulating tensor transport equations such as those in the differential stress models [35–37], which is the golden standard for RANS-based turbulence modeling [38]. The physics of Reynolds stress tensors are described by a set of nonlinear, coupled convection-diffusion-reaction type partial differential equations (PDEs) [39]. The tensor transport equations contain unclosed terms of even higher order statistics beyond the RANS equations, and calibrating an accurate closure term for the equations has been extremely difficult. Through the validation on a family of parameterized periodic hill geometries, we showcase that the proposed vector-cloud neural network with equivariance can be trained flexibly from data and meanwhile capture the nonlocal physics of tensor transport accurately. Among other potential applications, the work paves the way for further development towards frame-independent, nonlocal, data-driven Reynolds stress models based on neural networks.

C. Envisioned role of VCNN-e in turbulence modeling

The ultimate goal of this proposed framework is to emulate the transport equation of the normalized Reynolds stress anisotropy, which can be derived from the Reynolds stress transport equation to be presented in Section III and implies a similar region-to-point mapping as the latter does. It is not our intention to use VCNN-e to emulate the full Reynolds stress transport equations in turbulence modeling. It is well known that turbulence modeling consists of determining the length-scale, velocity-scale, and anisotropy of the turbulence. The former two quantities amount to eddy viscosity ν_t , which cannot be determined by the local mean flow (i.e., the mean velocity or its gradient). For example [40], the velocity gradients vanish at the center of a jet or channel flow but not the turbulence, while in slug flows both velocity gradient and turbulence vanish. Therefore, turbulent length- and velocity-scales must be solved for, i.e., via transport PDEs as in k - ε [41] and Spalart–Allmaras models [42]. These models account for the nonlocal dependence of eddy viscosity on the mean field. However, they do not account for the dependency of the Reynolds stress *anisotropy* on the mean flow upstream. Rather, the anisotropy is modeled based on local mean velocity gradient (or equivalently $\nabla \mathbf{u} = \mathbf{S} + \mathbf{\Omega}$). As such, eddy viscosity models (linear or nonlinear) are referred to as *weak equilibrium* models [18].

The VCNN-e is devised to emulate the nonlocal dependence of the normalized Reynolds anisotropy \mathbf{b} on the mean flow field. As a normalized quantity, the normalized anisotropy does not carry information of the turbulence length- and velocity-scales; the prediction of \mathbf{b} will complement the existing eddy viscosity models by providing a better description of the Reynolds stresses. Specifically, the VCNN-e based anisotropy model would enter a turbulence

modeling in the following way: (1) the VCNN-e mapping $\mathbf{b} = f_{\text{nn}}(\{\mathbf{u}\}_{i=1}^n)$ replaces the Boussinesq assumption or other point-based functions for reconstructing Reynolds stresses in traditional turbulence models; (2) the improved Reynolds stress appears as the production terms in the transport equations of turbulent kinetic energy and dissipation rate (or the corresponding transport PDEs for other turbulence models). The production term is of critical importance for accurately predicting these turbulent quantities. This is where several data-driven approaches anchor the uncertainty quantification of turbulence models [43] or machine learning-based augmentation thereof [44]. For strongly non-equilibrium flows the production term would deviate significantly from the linear eddy viscosity model prediction. The envisioned role of VCNN-e in the whole framework is summarized in Fig. 1. In the present work we focus on proving the concept of emulating a nonlinear, coupled tensor transport equation by using a nonlocal neural network with equivariance, VCNN-e. We choose the Reynolds stress transport equation with the LRR-IP model as our objective of emulation. However, note that such a choice is only made for convenience and does not represent the ultimate role of VCNN-e in turbulence modeling.

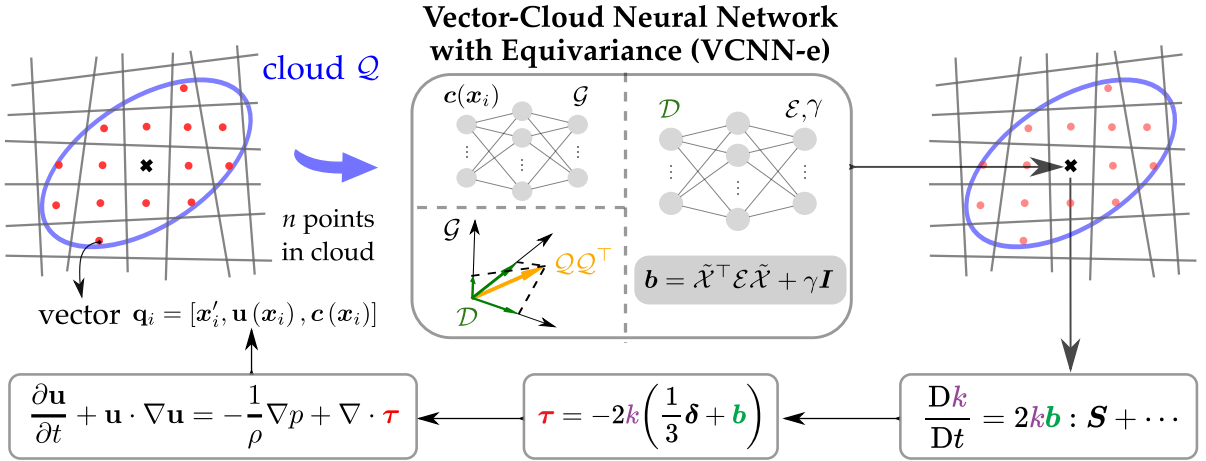


FIG. 1: Envisioned role of the proposed vector-cloud neural network with equivariance (VCNN-e) for emulating the transport equations of Reynolds anisotropy \mathbf{b} in a RANS solver with an eddy viscosity model consisting of transport equations of turbulence quantities (using turbulent kinetic energy k as example), and $\boldsymbol{\delta}$ is the Kronecker delta.

II. PROBLEM STATEMENT

We consider the Reynolds stress transport equation (i.e., with frozen velocity field) on the parameterized periodic hills. We adopt a simplified Reynolds stress transport equation with the LRR-IP model (a second-moment closure model of Launder, Reece, and Rodi with isotropization of production [39]). The frozen velocity field $\mathbf{u}(x)$ is obtained by using the k - ε eddy viscosity model [41], which is known for its robustness. As such the tensor transport equation for the Reynolds stress tensor \mathcal{R} can be written as

$$\frac{\partial \mathcal{R}}{\partial t} + \mathbf{u} \cdot \nabla \mathcal{R} - \nabla \cdot [(\nu_t + \nu) \nabla \mathcal{R}] = \mathcal{P} + \Phi - \mathcal{E}, \quad (1a)$$

where the left-hand side includes convection and diffusion, and the right-hand side consists of three tensors: production \mathcal{P} , pressure–strain-rate Φ , and dissipation tensor \mathcal{E} . The production term is closed, while the pressure–strain-rate tensor Φ consists of a slow component modeled by Rotta’s return-to-isotropy model and a rapid component modeled by the isotropization of production model [40]. These two terms can be written as follows:

$$\mathcal{P} = - [\mathcal{R} \cdot \nabla \mathbf{u} + (\mathcal{R} \cdot \nabla \mathbf{u})^\top], \quad (1b)$$

$$\Phi = \frac{C_1}{\tau} \text{dev}(\mathcal{R}) + C_2 \text{dev}(\mathcal{P}), \quad (1c)$$

where $\text{dev}(\cdot)$ indicates the deviatoric component of a tensor, “ \cdot ” denotes inner product between tensors, and $\tau = k/\varepsilon$ is the turbulence time scale. The dissipation tensor \mathcal{E} is assumed to be isotropic, i.e.,

$$\mathcal{E} = \frac{2}{3} \varepsilon \mathbf{I} \quad \text{with} \quad \varepsilon = C_D \frac{k^{3/2}}{\ell_m}, \quad (1d)$$

where \mathbf{I} is the second order identity tensor, and ε is the dissipation rate scalar estimated from the turbulence kinetic energy (TKE) $k \equiv \frac{1}{2} \text{tr}(\mathcal{R})$ and mixing length ℓ_m . ℓ_m is assumed to be proportional to wall distance η and capped by the boundary layer thickness δ^* , i.e.,

$$\ell_m = \min(\kappa\eta, C_\mu \delta^*) \quad (1e)$$

with von Karman constant $\kappa = 0.41$. Other model coefficients are chosen as $C_\mu = 0.09$, $C_D = C_\mu^{3/4}$, $C_1 = 1.8$, $C_2 = 0.6$. The boundary layer thickness is set based on the geometry for calculating the mixing length ℓ_m in equation (1e). Finally, the turbulent eddy viscosity is modeled by $\nu_t = C_\mu k^2/\varepsilon$.

We note that equations (1a)–(1e) by no means represent a complete differential Reynolds stress model, since many of the closure terms such as the diffusion and the dissipation are obtained with massively simplified models (comparable to those in incomplete one-equation models [40]). However, the equations capture much of the mathematical features of the Reynolds stress transport equation including convection, diffusion, production, and dissipation. Most importantly, it includes a model for the pressures–train-rate tensor, which is responsible for energy transfer among different components of the tensor \mathcal{R} . This tensor is notoriously difficult to model and is a pacing item in the development of differential Reynolds stress models.

So we treat equations (1a)–(1e) as a prototype closure model for the Reynolds stress \mathcal{R} . Instead of modeling and solving (1a)–(1e) to get the steady solution of \mathcal{R} , in this work we will construct and learn a nonlocal closure model to map from the velocity field to the stress tensor directly. We will use the above Reynolds stress transport equation on the parameterized periodic hills to generate data for training the neural network and test on geometry configurations that are similar but unseen in the training dataset.

III. METHODOLOGY

As motivated in the previous sections, we aim to construct a constitutive neural network to predict the Reynolds stress tensor \mathcal{R} at the point of interest \mathbf{x}_0 from the given flow field. Considering both the nonlocal physics embodied in the transport PDE (1a) and feasibility for implementation in CFD solvers, the network should form a region-to-point mapping $\langle \mathbf{q}(\mathbf{x}_0) \rangle \mapsto \mathcal{R}(\mathbf{x}_0)$, where \mathbf{q} is the feature vector (we always assume column vectors in this paper), and $\langle \mathbf{q}(\mathbf{x}_0) \rangle$ indicates the collection of features $\{\mathbf{q}_i\}_{i=1}^n$ on n points sampled from the region around \mathbf{x}_0 (referred to as *cloud*). The

extent of the cloud is determined by the velocity \mathbf{u} at the point of interest according to the region of physical influence (see the detailed expression in [33]). The number of points n in a cloud can vary from location to location so that our model should adapt to different discretizations. The feature vector \mathbf{q} attached to each point is chosen to include the relative coordinate $\mathbf{x}' = \mathbf{x} - \mathbf{x}_0$, flow velocity \mathbf{u} , and additional seven scalar quantities $\mathbf{c} = [\theta, \mathbf{u}, s, b, \eta, r, r']^\top$. These scalar features are the same as used in [33], and we briefly recall their definitions for completeness.

- (1) cell volume θ , which represents the weight for each point in mesh-based methods;
- (2) velocity magnitude $u = |\mathbf{u}|$ and strain rate magnitude $s = \|\mathbf{s}\| = \|\nabla\mathbf{u} + (\nabla\mathbf{u})^\top\|$, the latter of which often appears in various turbulence and transition models;
- (3) boundary cell indicator b and wall distance η after normalization by boundary layer thickness scale ℓ_δ and capped by 1. These two variables help the closure model to distinguish between the mapping described by the differential PDE and wall model (boundary condition);
- (4) proximity r (inverse of relative distance) to the center point of the cloud and proximity r' defined based on the angle between $-\mathbf{u}^\top$ and \mathbf{x}' accounting for the alignment between the convection and the relative position of the point in its cloud.

Note that all the input features are first non-dimensionalized by the characteristic length L_0 , flow velocity U_0 , and time $T_0 = L_0/U_0$, then fed into the neural network. As such the closure model can handle the dynamically similar systems with different scales. According to the above definition, the feature vector \mathbf{q} is $3 + 3 + 7 = 13$ dimensional, and we define the input data matrix as $\mathcal{Q} = [\mathbf{q}_1, \dots, \mathbf{q}_n]^\top \in \mathbb{R}^{n \times 13}$.

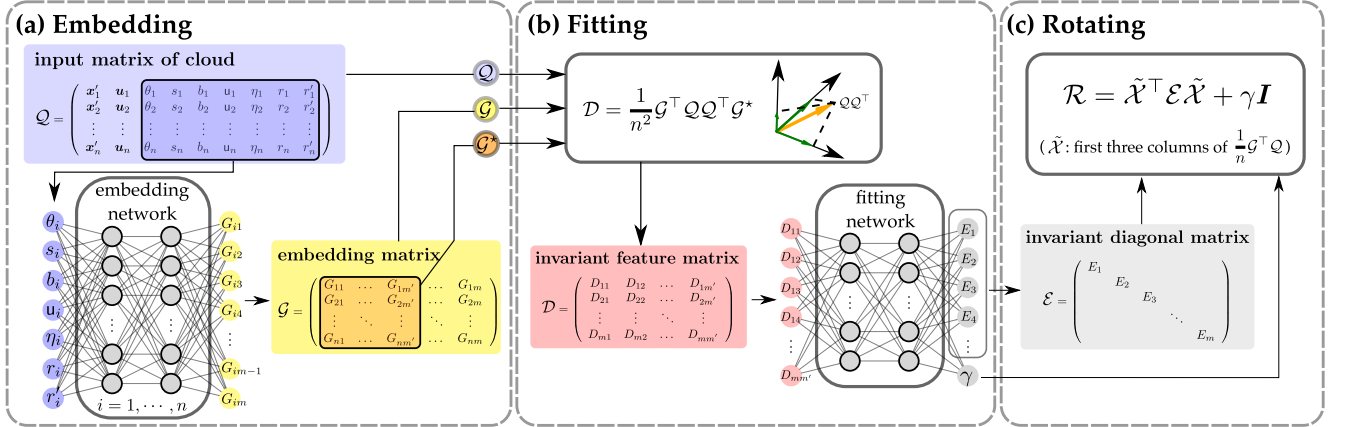


FIG. 2: Detailed schematic of the vector-cloud neural network with equivariance (VCNN-e) for predicting the nonlocal tensor \mathcal{R} : (a) embed the frame-independent features $\{\mathbf{c}_i\}_{i=1}^n$ to form the embedding matrix $\mathcal{G} \in \mathbb{R}^{n \times m}$; (b) project the pairwise inner-product matrix $\mathcal{Q}\mathcal{Q}^\top$ to the learned embedding matrix \mathcal{G}^\top and its submatrix \mathcal{G}^* to yield an invariant feature matrix $\mathcal{D} \in \mathbb{R}^{m \times m'}$; flatten and feed the feature matrix \mathcal{D} into the fitting network to predict the diagonal matrix \mathcal{E} and scalar γ ; (c) rotate \mathcal{E} through the embedded coordinates $\tilde{\mathcal{X}}$ and get the final predict of \mathcal{R} . The constitutive mapping $\mathbf{u}(\mathbf{x}) \mapsto \mathcal{R}$ based on the vector-cloud neural network is invariant to both the frame translation and the ordering of points in the cloud, and equivariant to the frame rotation.

The vector-cloud neural network with equivariance (VCNN-e) for modeling Reynolds stress tensor consists of three modules at a high level: an embedding module, a fitting module, and a rotating module. The goal of the first module (Fig. 2a) is to find a representation of the input data that is translational, rotational, and permutational invariant. To this end, we introduce a set of m basis functions $\{\phi_k(\mathbf{c}_i)\}_{k=1}^m$, implemented by an embedding neural network with m -dimensional output, for the scalar quantities \mathbf{c}_i (note the input \mathbf{c}_i is the frame-independent part of the feature vector \mathbf{q}_i) and define $\mathcal{L}_{kj} = \frac{1}{n} \sum_{i=1}^n \phi_k(\mathbf{c}_i) \mathcal{Q}_{ij}$, $k = 1, \dots, m, j = 1, \dots, 13$. The summation over the point index i removes the dependence of \mathcal{L} on the ordering and make it permutational invariant. The normalization by n allows different number of sampled points in the cloud in the training or testing data. If we define a matrix $\mathcal{G}_{ik} = \phi_k(\mathbf{c}_i)$, the permutation invariant transformation above can be written as $\mathcal{L} = \frac{1}{n} \mathcal{G}^\top \mathcal{Q}$. Similarly, we define $\mathcal{L}^* = \frac{1}{n} \mathcal{G}^{*\top} \mathcal{Q}$, with \mathcal{G}^* being the first m' columns of \mathcal{G} , and \mathcal{L}^* is also permutational invariant. Here we choose \mathcal{G}^* as a subset of \mathcal{G} instead of \mathcal{G} itself mainly in order to save the computational cost in the next step without sacrificing the accuracy. Next, we define $\mathcal{D} = \mathcal{L} \mathcal{L}^{*\top} = \frac{1}{n^2} \mathcal{G}^\top \mathcal{Q} \mathcal{Q}^\top \mathcal{G}^*$, which is translational, rotational, and permutational invariant since both \mathcal{L} and $\mathcal{L}^{*\top}$ are. We can view \mathcal{D} as a faithful extraction of information from the feature vectors in the cloud via projecting $\mathcal{Q} \mathcal{Q}^\top$ onto the learned basis \mathcal{G} . Then the second module (Fig. 2b) takes \mathcal{D} as the input and fit an invariant diagonal matrix \mathcal{E} . We construct a fitting network $f_{\text{fit}} : \mathcal{D} \mapsto [e_1, \dots, e_m, \gamma]^\top$ that maps \mathcal{D} to $(m+1)$ -dimensional output, and define a diagonal matrix $\mathcal{E} \in \mathbb{R}^{m \times m}$ taking e_1, \dots, e_m as the diagonal elements. Finally, in the third module (Fig. 2c), we re-incorporate the embedded coordinates $\tilde{\mathcal{X}} = \frac{1}{n} \mathcal{G}^\top \mathcal{X} \in \mathbb{R}^{m \times 3}$ from the first module where $\mathcal{X} = [\mathbf{x}_1, \dots, \mathbf{x}_n]^\top \in \mathbb{R}^{n \times 3}$ and rotate properly to get the final tensor prediction through

$$\mathcal{R} = \tilde{\mathcal{X}}^\top \mathcal{E} \tilde{\mathcal{X}} + \gamma \mathbf{I}. \quad (2)$$

Since $\tilde{\mathcal{X}}$ rotates in the same way as the original coordinates under rotation and \mathbf{I} is rotational equivariant, the final output \mathcal{R} preserves the desired equivariance. The optimal parameters in the embedding and fitting networks are trained from data. The detailed proof of equivariance property of the formulation in Eq. (2) is shown in Appendix A.

The formulation in Eq. (2) is inspired by the work of [34] in the context of molecular dynamics, which only has the first term $\tilde{\mathcal{X}}^\top \mathcal{E} \tilde{\mathcal{X}}$ satisfying the equivariance requirements. However, here we need to add an extra term $\gamma \mathbf{I}$ to ensure that the network correctly represents the function space and symmetries that are unique for turbulence modeling. Specifically, these requirements are:

- (1) The Reynolds stress tensor has a full rank three even for statistically two-dimensional (or even one- or zero-dimensional) mean flows, with all three diagonal components being nonzero in general. In contrast, the first part $\tilde{\mathcal{X}}^\top \mathcal{E} \tilde{\mathcal{X}}$ alone degenerates for such flows: it only has a rank of two for two-dimensional mean flows.
- (2) For two-dimensional mean flows, the out-of-plane stresses should be zero. This requirement is correctly satisfied by the first part $\tilde{\mathcal{X}}^\top \mathcal{E} \tilde{\mathcal{X}}$.

The additional term $\gamma \mathbf{I}$ enables the network to satisfy the first requirement of function space without breaking its equivariance property or the symmetries implied in the second requirement. Moreover, despite the apparent formal similarity of the formulation to the deviatoric decomposition of the Reynolds stress tensor, we note that our formulation is motivated mathematically rather than physically. Further details in the motivation and interpretation of the VCNN-e model are presented in Appendix B.

IV. RESULTS

In this work, we consider predicting the full Reynolds stress tensor modeled by equations (1a)–(1e) in the flows over periodic hills. We assume the flow is statistically homogeneous in the z -direction so that the z component of the mean velocity is 0. However, note that the instantaneous velocity fluctuations and thus the Reynolds normal stress in the z -direction is nonzero. The baseline configuration of the computational domain in the xy -plane (normal to z -axis) has the length $L_x/H = 9$ and the height $L_y/H = 3.035$, both of which are normalized by the crest height H , which is shown in Fig. 3a. The profile of the hill is described as piecewise polynomials with width $w/H = 1.93$. We systematically vary the slope parameter α of the hill profile to generate a family of geometry configurations for training and testing [45], as shown in Fig. 3b. The slope parameter α is defined as the ratio of the width w of the parameterized hill to that of the baseline hill $w|_{\alpha=1.0}$. The height of the hill remains the same for all configurations, and thus the hill gets more gentle with increasing slope parameter α . For training flows, we select 11 configurations with $\alpha = 1.0, 1.1, \dots, 2.0$. For testing flows, the slope parameters α are within the range from 0.5 to 4. The boundary layer thickness is set to be $\delta^*/H = 0.5$ for all cases.

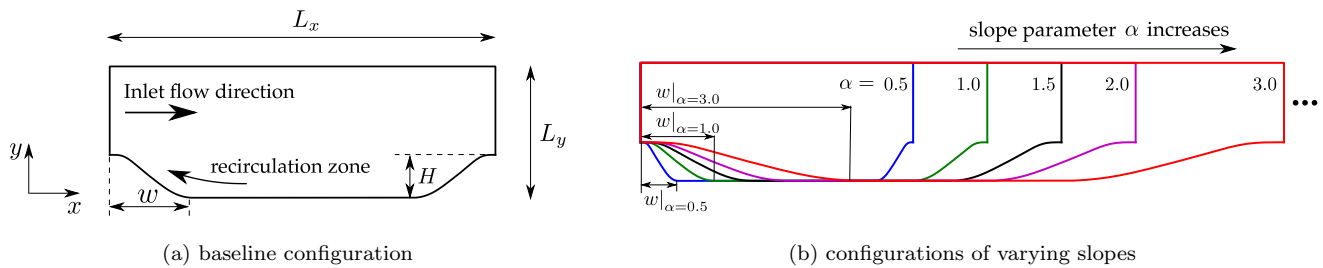


FIG. 3: Configurations of computational flow domains used for training and testing, showing (a) the baseline configuration in the xy -plane and (b) parameterized configurations with varying slopes parameters α , defined as the ratio of the width w of the hill to that of the baseline hill ($w|_{\alpha=1}$). The x - and y - coordinates are aligned with streamwise and wall-normal directions, respectively, and the z -coordinate is determined based on the right-hand rule (perpendicular to the paper and pointing outward). The slope parameters α are selected within the ranges $[1, 2]$ and $[0.5, 4]$ for training and testing flows, respectively.

A. Generation of training data

We calculate the steady Reynolds stress $\mathcal{R}(\mathbf{x})$ by solving the transport equation PDE (1a)–(1e) with a steady, incompressible flow field $\mathbf{u}(\mathbf{x})$. The flow in periodic hills is widely used as the benchmark to evaluate the performance of turbulence models for RANS simulations [46]. The flow is driven by a constant pressure gradient such that the Reynolds number based on the volume averaged bulk velocity magnitude u_b , the hill height H , and the the kinematic viscosity ν attains a specified value $Re = u_b H / \nu = 10595$. In this study, we perform all the numerical simulations in an open-source CFD platform OpenFOAM [47]. Firstly, we simulate the flows over the periodic hills by solving the RANS equations using the built-in steady-state incompressible flow solver simpleFoam, where the SIMPLE algorithm is applied [48]. Then, the calculated mean flow field and the corresponding Reynolds stress field are treated as the

frozen flow field and initial condition for solving the transport equation PDE (1a). When solving the RANS equations and the transport equation for Reynolds stress tensor, at both top and bottom walls non-slip boundary conditions ($\mathbf{u} = 0$) are applied for flow velocities and zero gradient boundary conditions ($\frac{\partial \mathcal{R}}{\partial n} = 0$) for the Reynolds stress tensors, while periodic boundary conditions are used in the streamwise direction. An unstructured-grid numerical discretization based on the finite volume method and second-order spatial discretization scheme is utilized to solve the equations. Specifically, we make the number of quadrilateral cells approximately proportional to the length L_x of the configuration in the x -direction (200 cells for the baseline configuration with $L_x/H = 9$), while in the y -direction the cells are refined towards the walls and the number is fixed at 200 for all configurations.

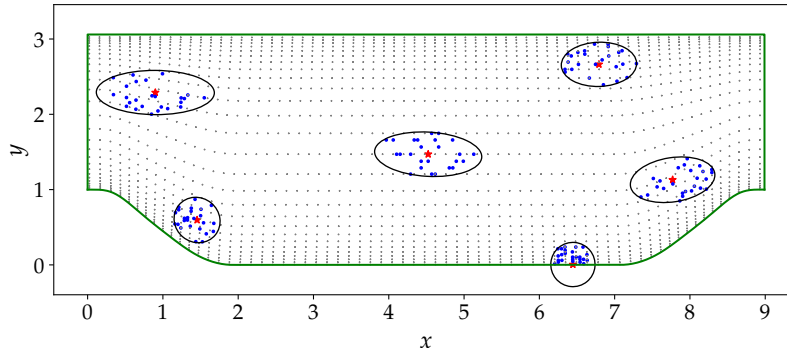


FIG. 4: Method of sampling data points within the cloud to generate pairs of labeled training data (\mathcal{Q}, \mathcal{R}). The gray dots (\bullet) indicate all the discrete points (i.e., the cell centers) within the computational domain, showing only every seventh row and third column for readability. The red star (\star) indicates the point of interest where the Reynolds stress tensor \mathcal{R} is to be predicted. The surrounding ellipse denotes the region of cloud, whose size and orientation are determined by the velocity at the cloud center (\star). The blue dots (\bullet) are randomly sampled within the cloud, and the set of all feature vectors attached to them is taken as the input matrix \mathcal{Q} to predict \mathcal{R} .

Our aim is to learn a region-to-point mapping from a patch of nonlocal mean flow field $\langle \mathbf{u}(\mathbf{x}) \rangle$ to the steady Reynolds stress tensor \mathcal{R} at the point of interest. As mentioned above, the nonlocal flow field is described by the input feature matrix \mathcal{Q} based on n points sampled from the cloud. The generation of such pairs of data (\mathcal{Q}, \mathcal{R}) in different locations is illustrated in Fig. 4. The grey dots (\bullet) indicate all the discrete points (i.e., the cell centers) within the computational domain, which are shown every seventh row and third column for readability; the red star (\star) indicates the point of interest at which the Reynolds stress tensor \mathcal{R} is to be predicted; n data points (\bullet) are randomly sampled within the vector cloud (\circ) to represent the nonlocal flow field used for prediction of the Reynolds stress tensor \mathcal{R} . We can see that the size and orientation of the elliptical cloud vary in different locations. The size of the ellipse is determined by the velocity magnitude $|\mathbf{u}|$ at the point of interest; the orientation (i.e., the major axis) of the ellipse aligns with the direction of the velocity \mathbf{u} . Specifically, the length ℓ_1 of the semi-major axis and ℓ_2 of the semi-minor axis are defined by the specified relative error tolerance $\epsilon (= 0.2)$ according to the previous work [49]:

$$\ell_1 = \left| \frac{2\nu \log \epsilon}{\sqrt{|\mathbf{u}|^2 + 4\nu\zeta} - |\mathbf{u}|} \right| \quad \text{and} \quad \ell_2 = \left| \sqrt{\frac{\nu}{\zeta}} \log \epsilon \right|, \quad (3)$$

where ν and ζ are diffusion and dissipation coefficients in the 1-D steady-state convection-diffusion-reaction equation $-\nu \frac{d^2}{dx^2} \tau(x) + u \frac{d}{dx} \tau(x) + \zeta \tau(x) = P(x)$. For the transport equation (1a) in this study, the actual dissipation coefficient

ζ in Eq. (3) should be approximately $\frac{2}{3}C_D\frac{k^{1/2}}{\ell_m}$, considering the dissipation term \mathcal{E} . Here, it is assumed as a constant $\zeta \approx 2$ to determine the size of the clouds, where the maximum ℓ_m and k are used for the approximation. Similarly, the actual diffusion coefficient ν in Eq. (3) is chosen as $(\nu_t + \nu)_{\min} \approx 0.01$.

After determining the size of clouds, we randomly sample $n = 300$ data points within each cloud to generate training data. The available data points are repeatedly sampled for the locations where the number of data points in the ellipse is smaller than 300. It should be noted that the proposed neural network is flexible with an arbitrary number of sampled points in the cloud. Here we set n as a constant for training in order to store the data conveniently and process them in batches for better computational efficiency during training. There are 6.6×10^5 pairs of $(\mathcal{Q}, \mathcal{R})$ in total for 11 training flows with $\alpha = 1.0, 1.1, \dots, 2.0$. Considering the adjacent data pairs from the same flow appear similar, we take one from every two adjacent pairs to reduce the size of the training dataset and finally use 3.3×10^5 pairs of $(\mathcal{Q}, \mathcal{R})$ as the training data.

B. Neural-network-based prediction of Reynolds stress tensors

After generating the training data, we use the squared difference between the predicted stress and the ground truth as the loss function and train the proposed VCNN-e model. It is straightforward to train the model directly using the data described above. Here, however, another progressive training method is used to improve the training efficiency considering that VCNN-e is flexible with an arbitrary number of sampled points in the cloud. Specifically, we first train the neural network for 1000 epochs based on a subset of the training data with only $n = 25$ sampled points in the cloud (i.e., sparse data) and then 4000 epochs using the full generated training data with $n = 300$ sampled points (i.e., dense data). Such a progressive training method starting with sparse data can significantly reduce the training time (close to 18%) when compared to the direct training using dense data for 5000 epochs (11.12 and 13.56 seconds per epoch on average, respectively), and it turns out the progressive training method achieves better performance due to the acceleration of the optimization process. A detailed comparison of these two training methods is provided in Appendix C. The training processes are performed on an NVIDIA RTX 3090 GPU using the open source machine learning framework PyTorch [50]. The code for data generation and model training are both available on GitHub [51], which can be used by the readers for reproducing the results and further development.

After training, the prediction capabilities of the well-trained neural-network-based model are investigated in different configurations with slope parameters α between 0.5 and 4. For the testing step, we take all the data points within the clouds (approximately 50 to 2000 points) to predict the Reynolds stress tensor at the cloud centers, which is different from using only 300 sampled points in each cloud for prediction in the training step. In this study, we examine how well the learned model performs toward capturing two types of quantities: (1) turbulence kinetic energy (TKE) k and Reynolds stress anisotropy invariant A_2 , both of which are invariants of the Reynolds stress tensor, and (2) Reynolds shear stress component \mathcal{R}_{xy} . Note that the Reynolds stress components, including the shear component evaluated here, are included in the definition of the loss function of the network, but the invariant quantities such as the TKE and the anisotropy scalar A_2 (detailed below) are not included. Accurate predictions of these invariant quantities rely on the equivariant property of the proposed VCNN-e model.

We first calculate the TKE k based on the predicted Reynolds stress tensors and then compare the predicted TKE with the corresponding ground truths. The TKE is defined as half the trace of the Reynolds stress tensor:

$k = \frac{1}{2} \text{tr}(\mathcal{R}) = \frac{1}{2}(\mathcal{R}_{xx} + \mathcal{R}_{yy} + \mathcal{R}_{zz})$, which determines the magnitude of Reynolds stress isotropy tensor. The comparisons for two extreme interpolated flows with $\alpha = 1$ and $\alpha = 2$ are shown in Fig. 5. Note that due to the different sampled points in the clouds, there could be considerable differences between the inputs of training and testing data even for the flows of the same slope parameter α . According to Fig. 5(a)–(d), we can see that the predicted TKE fields are nearly identical to the corresponding ground truths for both interpolated testing flows. The comparisons are visualized more clearly in Fig. 5(e)–(f), showing that the profiles of the predicted TKE over the vertical cross-sections almost coincide with those of the corresponding ground truths. Such good prediction performance in the interpolated testing flows is to be expected; the success lies in the fact that the randomly sampled 300 data points in each cloud for training are representative enough to describe the nonlocal flow field, and thus the trained model can use the knowledge learned from the sampled points in the training data to use feature vectors attached to those unseen data points in the testing data to make a good prediction.

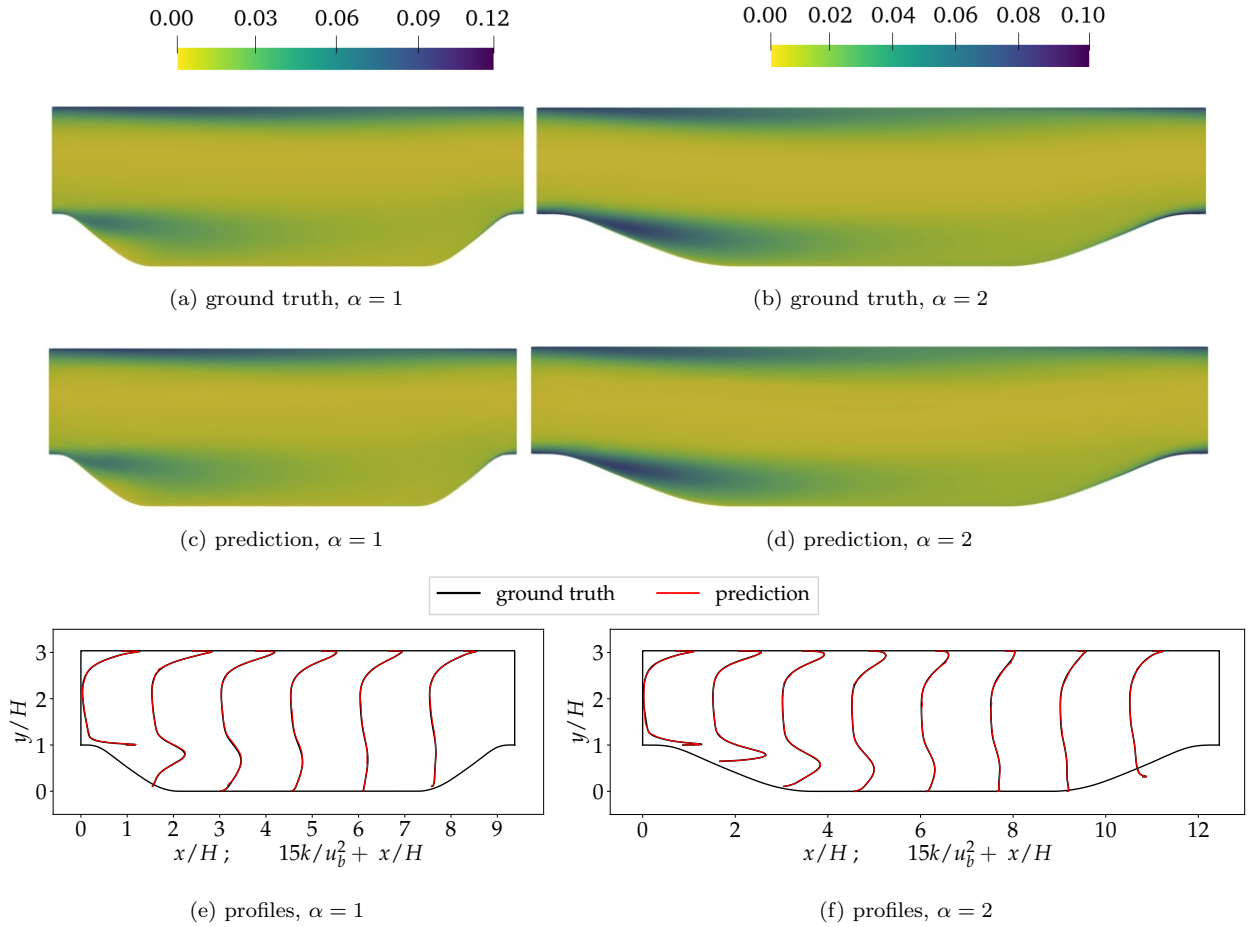


FIG. 5: Comparison of the ground truths of the **turbulence kinetic energy** (TKE) k (top row) and the corresponding predictions based on the predicted Reynolds stress with the trained neural network (middle row), along with the TKE profiles at six and eight cross-sections (bottom row) for two **interpolated** configurations with slope parameters $\alpha = 1$ (left panels) and $\alpha = 2$ (right panels).

Moreover, the trained model is tested on two extreme extrapolated flows with $\alpha = 0.5$ and $\alpha = 4$, which is shown in Fig. 6. From Fig. 6(a)–(d), we can see in the extrapolated flows, the trained model does not perform as well as

it does in the interpolated flows. For the flow with $\alpha = 0.5$, there are some inconsistency and roughness despite the overall similarity. The discrepancy is illustrated more clearly in Fig. 6(e), the comparison of the predicted and true TKE profiles on seven vertical cross-sections ($x/H = 0, 1, \dots, 6$). The most remarkable deviations are just behind the hill and near the inlet, which is perhaps caused by the stronger flow separation and larger recirculation zone due to the steeper slope of the hill. For flow with $\alpha = 4$, the prediction of TKE seems much better and closer to the ground truth in spite of some subtle differences, which is mainly because of the gentle slope and resulting mild change of flow field compared to the training flows. Such prediction performance in flows with $\alpha = 0.5$ and 4 is reasonable as extrapolating highly nonlinear functions to new flows that are far away from the training flows can be a very challenging task.

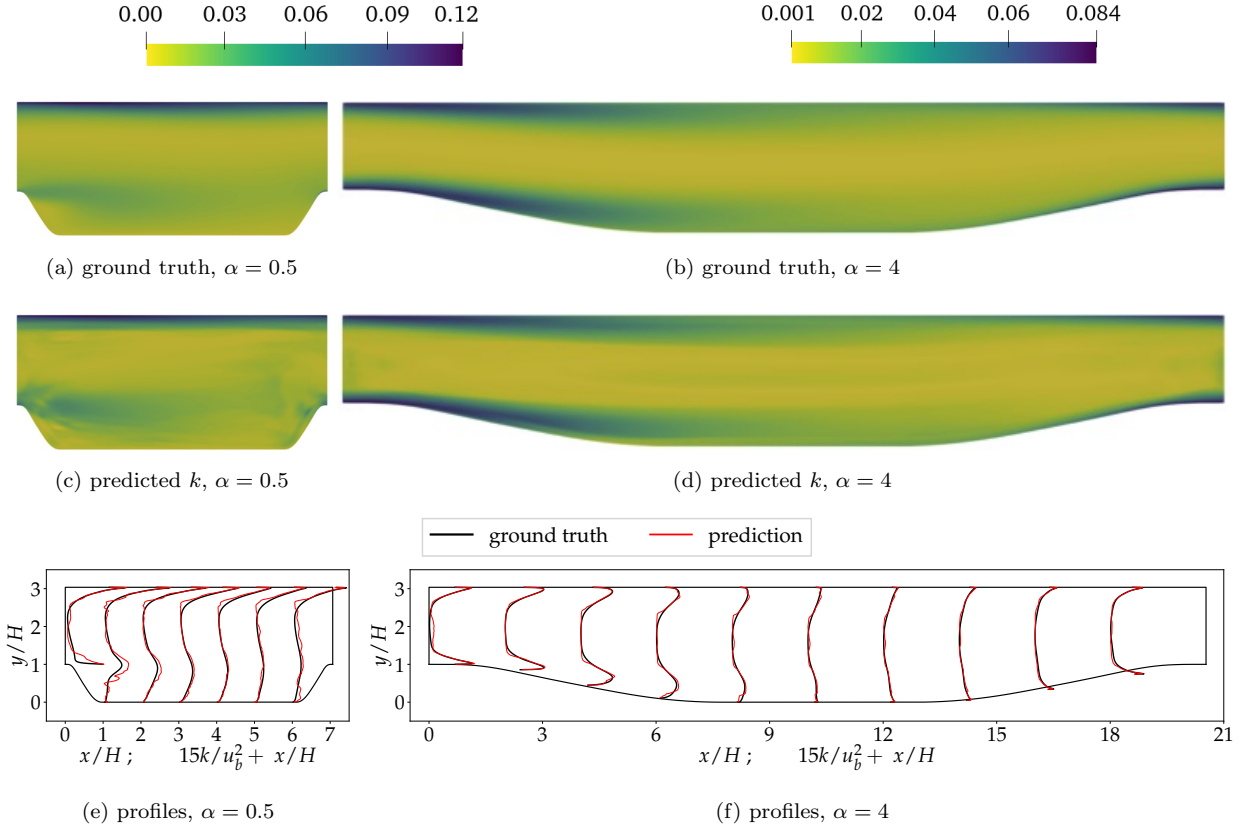


FIG. 6: Comparison of the ground truths of the **turbulence kinetic energy** k (top row) and the corresponding predictions based on the predicted Reynolds stress with the trained neural network (middle row), along with the TKE profiles at seven and ten cross-sections (bottom row) for two extreme **extrapolated** configurations with slope parameters $\alpha = 0.5$ (left panels) and $\alpha = 4.0$ (right panels).

Another evaluation criterion of predictive capability considered in this work is the Reynolds stress anisotropy invariant A_2 as in practical flows the Reynolds stress tensor is anisotropic due to deformation of large eddies by mean strain, inhomogeneities and boundaries. The predicted invariant A_2 is half the square of the tensor magnitude of the normalized Reynolds stress anisotropy \mathbf{b} computed as [52]:

$$A_2 = b_{ij}b_{ji}/2, \quad \text{with } b_{ij} = \frac{\mathcal{R}_{ij}}{2k} - \frac{1}{3}\delta_{ij}, \quad (4)$$

where k is the TKE and δ_{ij} is the Kronecker delta. In this work, we scale the invariant A_2 by the TKE k , considering that A_2 of anisotropy tensor is no longer important when k is sufficiently small. The predictions of scaled A_2 are then compared with the corresponding ground truths in both interpolated and extrapolated flows. Similarly, the predictions in flows with $\alpha = 1$ and 2 are quite accurate with almost no difference compared to the ground truths, which is shown in Fig. 12 in Appendix D. For extrapolated flows, however, things could be different as the squaring operation in the definition of A_2 may bring to larger prediction error. From Fig. 7(a) and (c), we can see in the flow with $\alpha = 0.5$, the regions with obvious prediction inconsistency are still near the center part of the recirculation zone and close to the hill, which is illustrated more clearly on seven cross-sections in Fig. 7(e) with a 50 times magnification. In the flow with $\alpha = 4$, the predictions of scaled A_2 are much better despite some minor fluctuations, which is shown in the right panels of Fig. 7. This is because there is almost no flow separation due to the gentle slope and the mean flow field near the hill is more similar to that in the near (bottom) wall region.

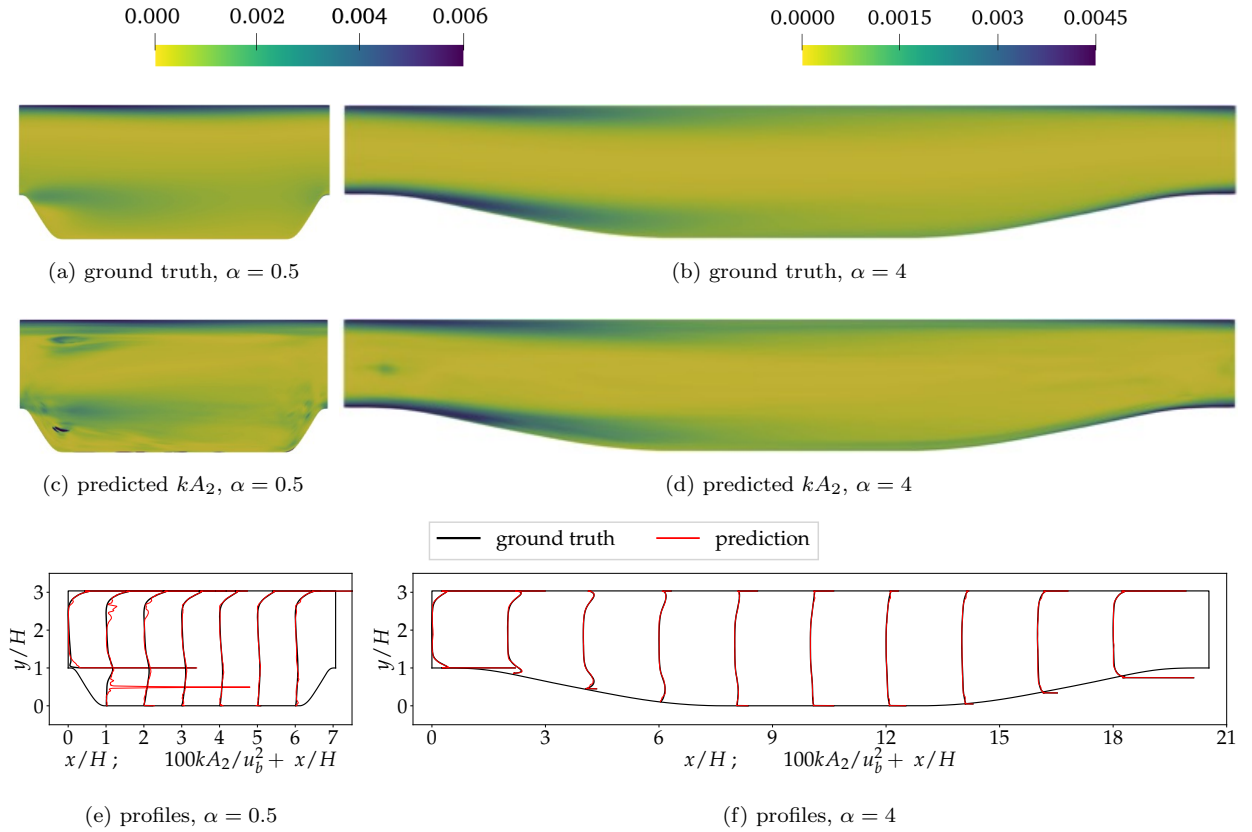


FIG. 7: Comparison of the ground truths of kA_2 , the **Reynolds stress anisotropy invariant** scaled by the turbulent kinetic energy (top row) and the corresponding predictions based on the predicted Reynolds stress with the trained neural network (middle row), along with the scaled A_2 profiles at seven and ten cross-sections (bottom row) for two extreme **extrapolated** configurations with slope parameters $\alpha = 0.5$ (left panels) and $\alpha = 4.0$ (right panels).

Besides the turbulent kinetic energy k and anisotropy invariant A_2 , we also examine the predicted Reynolds shear stress component \mathcal{R}_{xy} in the testing flows. Note that unlike the previous two quantities that are not included as training labels in the loss function, \mathcal{R}_{xy} is part of training labels and used directly in the loss function. It turns out that the qualitative results of the comparison for \mathcal{R}_{xy} is quite similar to those of k and A_2 : in the interpolated flows

with $\alpha = 1$ and 2, the predicted \mathcal{R}_{xy} show excellent agreement with the ground truths, while in the extrapolated flows with $\alpha = 0.5$ and 4, some deviations are observed, especially in the steepest case of $\alpha = 0.5$. We provide figures showing the detailed comparison in Appendix D.

In addition, we evaluate the generalizability of the trained model on 21 configurations with varying slope parameters α between 0.5 and 4. The prediction errors of all the testing flows are shown in Fig. 8. The prediction error is defined as the normalized L₂-norm discrepancy between the calculated TKE \hat{k} based on the predicted Reynolds stress tensor and corresponding ground truth k^* :

$$\text{error} = \frac{\sqrt{\sum_{i=1}^N |\hat{k}_i - k_i^*|^2}}{\sqrt{\sum_{i=1}^N |k_i^*|^2}}, \quad (5)$$

where the summation is performed on all of the N training or testing data points (e.g., 40000 data points for baseline configuration with $\alpha = 1$). Again, the prediction is performed using all the points within the cloud, which is different from the fixed number of sampled points in the training data. In Fig. 8, the middle (yellow/light gray) region from 1 to 2 represents the regime of slope parameters α of training flows while the region on both sides (blue/dark) represent the regime of the testing flows. We can see the performances of trained model on 11 interpolated testing flows ($\alpha = 1, 1.1, \dots, 2$) are the best with the prediction errors all around 1.8%, showing the learned model can accurately describe the transport of Reynolds stress tensors. When extrapolating to flows with steeper ($\alpha < 1$) or more gentle ($\alpha > 2$) hill profiles, the prediction errors increase significantly to 14.67% for $\alpha = 0.5$ and 8.69% for $\alpha = 4$, which is still reasonable because the Reynolds stress tensor is highly sensitive to the flow separation and thus easily influenced by the hill profile.

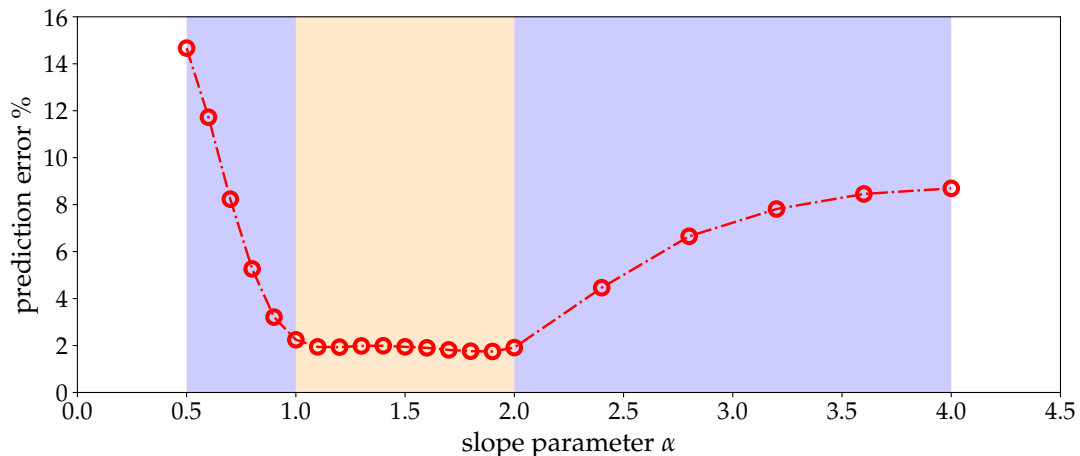


FIG. 8: General predictive errors for turbulence kinetic energy k at various slope parameters α . The yellow/lighter and blue/darker backgrounds represent the regimes of the slope parameters α of training and testing flows, respectively. The neural network is trained with data from 11 configurations with $\alpha = 1, 1.1, \dots, 2$. The trained network is then tested on the same 11 configurations with different inputs in the training regime and 10 configurations with $\alpha = 0.5, 0.6, \dots, 0.9$ and $\alpha = 2.4, 2.8, \dots, 4$ in the testing regime.

Such interpolation and extrapolation performance can be further explained by the data distribution of the training and testing flows. The difference of data distribution in two directions of extrapolation is visualized through the

scatter plot of the variable pairs with different α : velocities in x/y -directions (u/v) in Fig. 9, and turbulence kinetic energy k /anisotropy invariant A_2 in Fig. 10. We can see that in subfigure (a), the interpolation regime, both the input data u, v and output-dependent data k, A_2 have similar distributions as α change values from 1 to 1.5, and to 2. In subfigure (c), the data distribution corresponding to $\alpha = 4$ keeps the trend of change and deviates from the interpolation data a little bit. In contrast, in subfigure (b), the data distribution corresponding to $\alpha = 0.5$ presents some data points that are more significantly away from the training data.

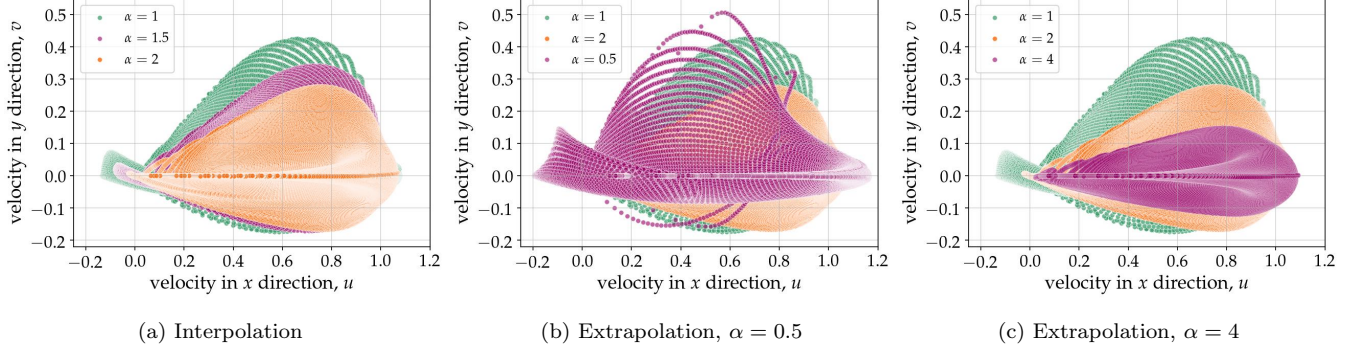


FIG. 9: Scatter plot of the joint data distribution of the velocities in x/y directions (u/v) with different slope parameters α , in the regimes of interpolation and extrapolation on two sides.

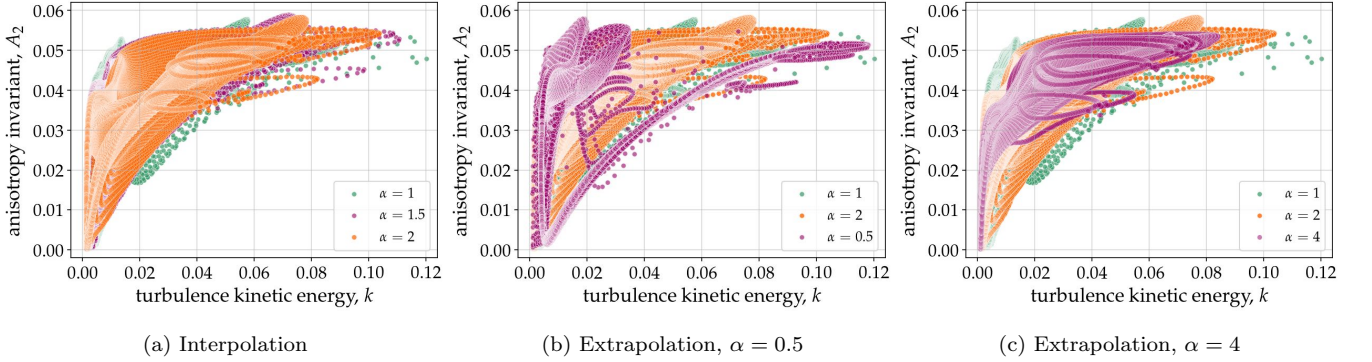


FIG. 10: Scatter plot of the joint data distribution of the turbulence kinetic energy k and anisotropy invariant A_2 with different slope parameters α , in the regimes of interpolation and extrapolation on two sides.

V. CONCLUSION AND FUTURE WORKS

In this work we generalize the vector-cloud neural network to model the constitutive tensor transport equations. By training on unstructured data points, the proposed network can faithfully capture the underlying nonlocal physics through a region-to-point mapping; it is invariant to coordinate translation and ordering of the points and meanwhile equivariant to coordinate rotation. The demonstrated performance shows its promise for nonlocal constitutive models, especially the RANS momentum equation in turbulence modeling to solve for mean velocities and pressure. The

immediate next step is to examine the performance of the learned nonlocal model as the closure model for the primary PDEs. We also note that, unlike the original RANS equations, the considered equations in this work are uncoupled with the momentum equations, i.e., the velocity field is frozen and unaffected by the Reynolds stress field. We will evaluate the performance of learning a nonlocal closure model from the fully coupled RANS equations and closure PDEs. Furthermore, we will evaluate the proposed network on more complicated, three-dimensional flows. Finally, current input only used vectors; how to include tensor quantities (e.g., strain-rate and rotation-rate) of the mean flow in the input for nonlocal constitutive modeling is an interesting question to explore in future work.

ACKNOWLEDGMENTS

The computational resources used for this project were provided by the Advanced Research Computing (ARC) of Virginia Tech, which is gratefully acknowledged.

Appendix A: Equivariance of the proposed vector-cloud neural network

We claim that the proposed network has rotational equivariance. That is, given a function $\mathcal{R} = f(\mathbf{q})$ where \mathbf{q} is the input of vector type and \mathcal{R} is the output of tensor type, we say f is equivariant if the following equation holds for any rotation matrix \mathbf{Q} :

$$\mathbf{Q}\mathcal{R}\mathbf{Q}^\top = f(\mathbf{Q}\mathbf{q}) \quad \text{or more concisely} \quad \mathcal{R}' = f(\mathbf{q}'),$$

in which the prime denote vector or tensor under the rotated frame. Here we demonstrate that a function of the following form satisfies the equivalence condition above:

$$\mathcal{R} = \mathcal{X}^\top \mathcal{E} \mathcal{X} + \gamma \mathbf{I} \tag{A1}$$

where \mathbf{I} is a second order identity tensor, \mathcal{X} are vectors defined in the same coordinate system as \mathbf{q} and \mathcal{R} , and \mathcal{E} is a function with tensor output that is *invariant* with the input vector \mathbf{q} , i.e., $\mathcal{E}(\mathbf{q}) = \mathcal{E}(\mathbf{q}')$. We first note the fact that the identity tensor is equivariant under rotation, i.e., $\mathbf{Q}\mathbf{I}\mathbf{Q}^\top = \mathbf{I}$. The equivariance can be shown straightforwardly as follows:

$$\mathbf{Q}\mathcal{R}\mathbf{Q}^\top = \mathbf{Q}\mathcal{X}^\top \mathcal{E} \mathcal{X}\mathbf{Q}^\top + \gamma \mathbf{I} = (\mathbf{Q}\mathcal{X})^\top \mathcal{E} (\mathbf{Q}\mathcal{X}) + \gamma \mathbf{I}. \tag{A2}$$

Or more concisely:

$$\mathcal{R}' = \mathcal{X}' \mathcal{E} \mathcal{X}'^\top + \gamma \mathbf{I}.$$

That is, the function form proposed in Eq. (A1) holds in the rotated frame for any rotation \mathbf{Q} .

Appendix B: Interpretation and symmetries of proposed formulation

This formulation of Reynolds stress $\mathcal{R} = \mathcal{X}^\top \mathcal{E} \mathcal{X} + \gamma \mathbf{I}$ is apparently similar to the deviatoric–hydrostatic (anisotropic–isotropic) decomposition frequently used in turbulence modeling [40]:

$$\mathcal{R} \equiv \overline{u_i u_j} = 2k \left(\mathbf{b} + \frac{\mathbf{I}}{3} \right) = 2k \left(\mathbf{V} \Lambda \mathbf{V}^\top + \frac{\mathbf{I}}{3} \right) \tag{B1}$$

where k is the turbulent kinetic energy (half the trace of \mathcal{R}), $\mathbf{b} = \text{dev}(\mathcal{R})/2k$ is the normalized anisotropy, and Λ and \mathbf{V} are eigenvalues and eigenvectors of tensor \mathbf{b} . However, it is worth noting that the two forms are fundamentally different. First, the decomposition is a mathematical construction to guarantee rotational equivariance. It is not motivated physically. Second, the mathematical structures of the two decompositions are also different. Most notably, the deviatoric tensor \mathbf{a} has zero trace by construction, while $\mathcal{X}^\top \mathcal{E} \mathcal{X}$ has nonzero trace. Also note that for flows aligned with the xy -plane (normal to z -axis), the xz -, yz -components of the part $\mathcal{X}^\top \mathcal{E} \mathcal{X}$ are zeros, while both components are nonzero in general for the normalized anisotropic tensor \mathbf{b} .

It can be seen from the derivation above that a formulation containing only the first part, i.e., $\mathcal{R} = \mathcal{X}^\top \mathcal{E} \mathcal{X}$, would be sufficient to guarantee equivariance of the formulation. Unfortunately, it fails to represent a correct function space for modeling Reynolds stresses in plane mean-strain conditions (i.e., statistically one- or two-dimensional mean flows). As such, the isotropic part $\gamma \mathbf{I}$ is added to the formulation to address the functional space mismatch problem, which is further detailed below.

Without loss of generality, consider a turbulent flow with the two-dimensional mean flow in the xy -plane (i.e., the z -direction is statistically homogeneous and thus has zero strain-rate). The z -component of the relative coordinates \mathcal{X} is zero. In this case simple algebra shows that the tensor $\mathcal{X}^\top \mathcal{E} \mathcal{X}$ has the following form:

$$\begin{bmatrix} \mathcal{R}_{xx} & \mathcal{R}_{xy} & 0 \\ & \mathcal{R}_{yy} & 0 \\ \text{symm} & & 0 \end{bmatrix}$$

It is noteworthy that by construction the formulation correctly ensures that (1) the output is a symmetric tensor and (2) that the shear components \mathcal{R}_{xz} and \mathcal{R}_{yz} terms are zero in such two-dimensional mean flows. However, the normal stress component \mathcal{R}_{zz} is also forced to zero, while in general this term is nonzero even in statistically two-dimensional flows (or even in the simplest isotropic homogeneous flows). For example, it has been shown by experiments that the ratios of normal stress components (i.e., turbulence intensities) in the streamwise (x -), wall-normal (y -), and spanwise (z -) directions are $\mathcal{R}_{xx} : \mathcal{R}_{yy} : \mathcal{R}_{zz} \approx 1 : 0.4 : 0.6$ in the log-law region of a zero-pressure gradient flat-plate boundary layer [53].

One would be tempted to remedy the inadvertent singularity by generating the training data in a general plane (i.e., by rotating the coordinate frame so that the flow is not aligned with the xy -plane). However, this is not a valid workaround. Since the formulation is rotational equivariant by construction, no matter in which coordinate system the training is performed, the trained model will still predict $\mathcal{R}_{zz} = 0$ if the flow is aligned with the xy -plane, which violates the physics discussed above.

There is also another perspective to understand the inadequacy of the term $\mathcal{X}^\top \mathcal{E} \mathcal{X}$. When the z -component of the relative coordinate \mathcal{X} is always zero, \mathcal{X} 's row space is at most two-dimensional. Note that the row space of $\mathcal{X}^\top \mathcal{E} \mathcal{X}$ is no larger than that of \mathcal{X} , i.e., it has a rank of no more than two. In contrast, the physical Reynolds stress has a full rank (i.e., of three) in general even for statistically one- or two-dimensional mean flows. Hence, the formulation $\mathcal{R} = \mathcal{X}^\top \mathcal{E} \mathcal{X}$ cannot adequately represent Reynolds stresses in one- or two-dimensional mean flows.

In view of such difficulties, we propose to add a term that allows the \mathcal{R}_{zz} component to be nonzero, while preserving the equivariance of the first part ($\mathcal{X}^\top \mathcal{E} \mathcal{X}$) as well as the existing symmetries of the output tensor (i.e., $\mathcal{R}_{yz} = \mathcal{R}_{zy} = 0$ and $\mathcal{R} = \mathcal{R}^\top$). The term $\gamma \mathbf{I}$ satisfies all these requirements. Note that here γ is a trainable scalar parameter as

opposed to $2k/3$ in the anisotropic decomposition Eq. (B1). Finally, because the formulation is equivariant, such a construction is a valid remedy regardless of the direction of the plane strain.

Appendix C: Progressive training of neural networks

In this work, we have explored two training methods: (1) direct training always using dense data, each having $n = 300$ points in the cloud, and (2) progressive training first with sparse data ($n = 25$ points in the cloud) and then dense data. In the first method, we directly train the model with 5000 epochs. In the second method, we first train using the sparse data with 1000 epochs and then using the full data with 4000 epochs. As pointed out in the main text, under the same number of epochs, the second method saves about 18% training time compared to the first method. The prediction performances of the trained models under two different methods are compared over 21 different configurations, which is shown in Fig. 11. We can see that, with less training time, the progressive method performs better in all testing cases. This is because the first stage of training using sparse data (i.e., a subset of full training data) accelerates the convergence of the neural-network-based model.

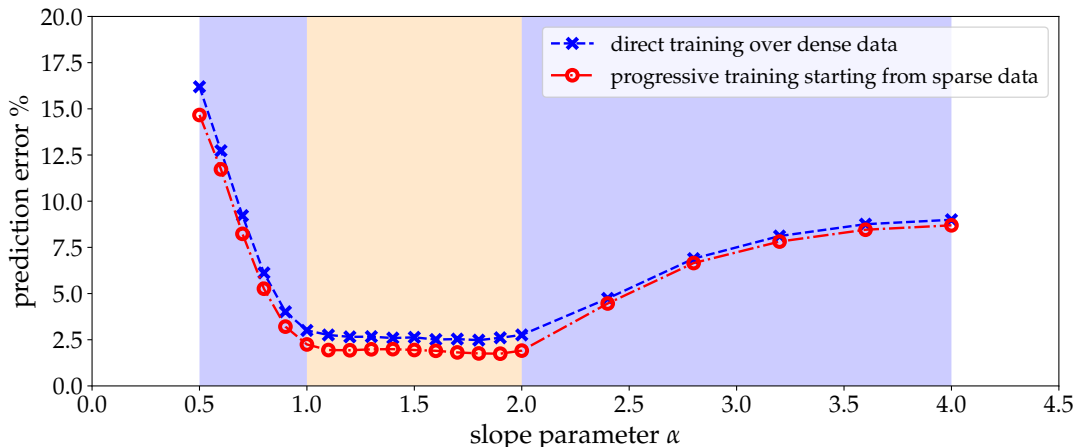


FIG. 11: Comparison of direct and progressive training methods in terms of prediction performance for turbulence kinetic energy k at various slope parameters α between 0.5 and 4. The blue dashed and red dash-dotted lines represent the prediction errors of the trained models by direct and progressive training methods, respectively. The testings on 21 flows are based on all the data points within the cloud, and thus the comparison is fair.

Appendix D: Additional predictions of Reynolds shear stress and anisotropy invariant

Additional results on the predictions of Reynolds shear stress \mathcal{R}_{xy} and anisotropy invariant A_2 are placed in this appendix as they show the same general trend as those in Section IV B while providing some additional evidence on the performance of the proposed method.

The predicted Reynolds stress anisotropy invariant A_2 in interpolated flows is calculated based on the corresponding predicted Reynolds stress and then compared to the ground truth, which is shown in Fig. 12. As expected, these

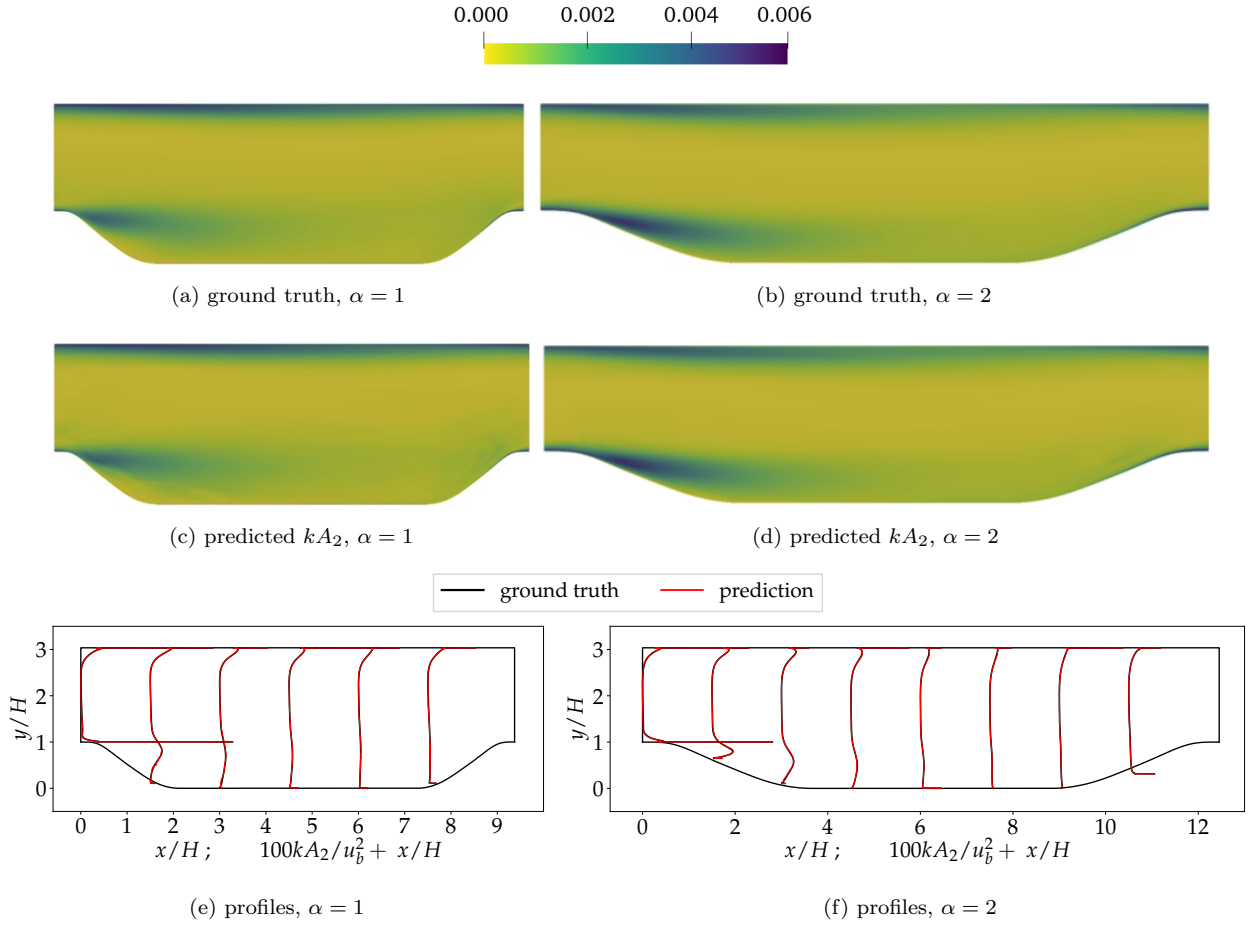


FIG. 12: Comparison of the ground truths of kA_2 , the **Reynolds stress anisotropy invariant** scaled by the turbulent kinetic energy (top row) and the corresponding predictions based on the predicted Reynolds stress with the trained neural network (middle row), along with the scaled A_2 profiles at several cross-sections (bottom row) for two **interpolated** configurations with slope parameters $\alpha = 1$ (left panels) and $\alpha = 2$ (right panels).

results are much better than those presented in Fig. 7 as the predicted slope is contained within the training data $\alpha \in [1, 2]$.

The predicted Reynolds shear stress component \mathcal{R}_{xy} in interpolated and extrapolated flows are shown in Fig. 13 and Fig. 14, respectively. The prediction performances are consistently good in two extreme interpolated flows with $\alpha = 1$ and 2. For extrapolated flow with $\alpha = 0.5$, the steepest slope makes it difficult to predict \mathcal{R}_{xy} accurately in the recirculation zone. Nevertheless, the prediction gets apparent improving compared to those of TKE k and Reynolds stress anisotropy invariant A_2 . This is because \mathcal{R}_{xy} is a component of Reynolds stress tensor and included in the definition of the loss function to learn the model.

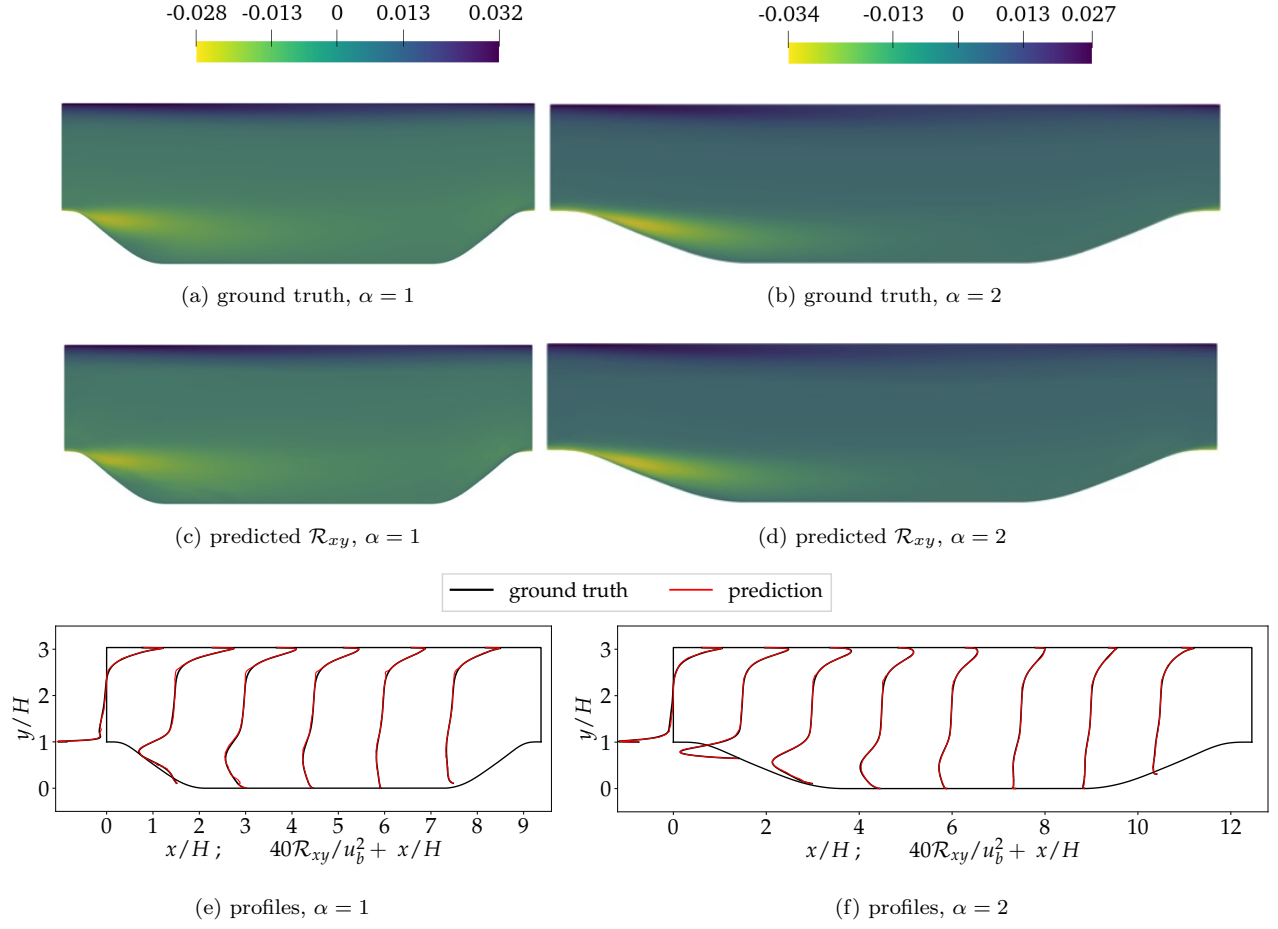


FIG. 13: Comparison of the ground truths of the **shear component of Reynolds stress** \mathcal{R}_{xy} (top row) and the corresponding predictions with the trained neural network (middle row), along with the \mathcal{R}_{xy} profiles at several cross-sections (bottom row) for two **interpolated** configurations with slope parameters $\alpha = 1$ (left panels) and $\alpha = 2$ (right panels).

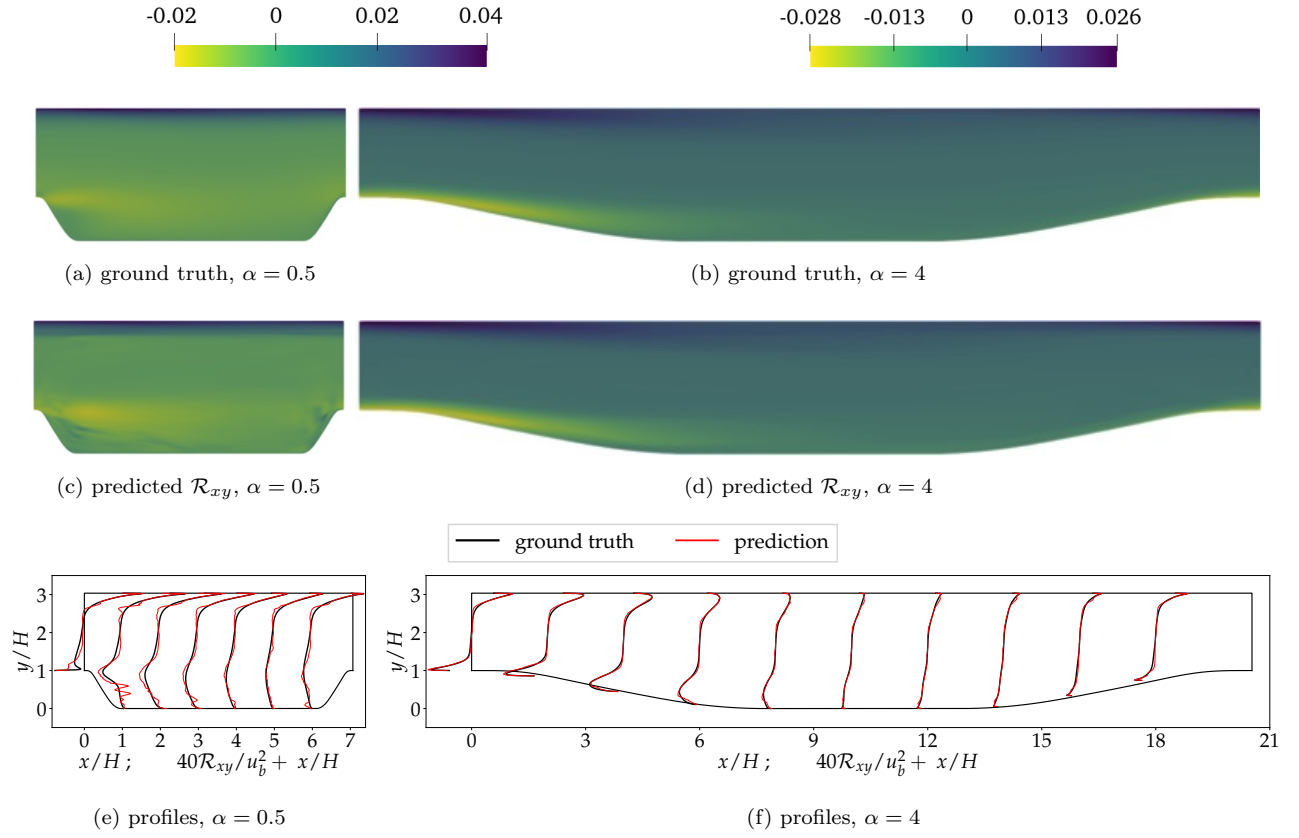


FIG. 14: Comparison of the ground truths of the **shear component of Reynolds stress** \mathcal{R}_{xy} (top row) and the corresponding predictions with the trained neural network (middle row), along with the \mathcal{R}_{xy} profiles at several cross-sections (bottom row) for two extreme **extrapolated** configurations with slope parameters $\alpha = 0.5$ (left panels) and $\alpha = 4.0$ (right panels).

-
- [1] A. P. Singh, S. Medida, and K. Duraisamy, Machine learning-augmented predictive modeling of turbulent separated flows over airfoils, *AIAA Journal* **55**, 2215 (2017).
- [2] J. Ling, A. Kurzawski, and J. Templeton, Reynolds averaged turbulence modelling using deep neural networks with embedded invariance, *Journal of Fluid Mechanics* **807**, 155 (2016).
- [3] J.-X. Wang, J.-L. Wu, and H. Xiao, Physics-informed machine learning approach for reconstructing Reynolds stress modeling discrepancies based on DNS data, *Physical Review Fluids* **2**, 034603 (2017).
- [4] J.-L. Wu, H. Xiao, and E. G. Paterson, Physics-informed machine learning approach for augmenting turbulence models: A comprehensive framework, *Physical Review Fluids* **3**, 074602 (2018).
- [5] X. I. A. Yang, S. Zafar, J.-X. Wang, and H. Xiao, Predictive large-eddy-simulation wall modeling via physics-informed neural networks, *Physical Review Fluids* **4**, 034602 (2019).
- [6] M. Schmelzer, R. P. Dwight, and P. Cinnella, Discovery of algebraic reynolds-stress models using sparse symbolic regression, *Flow, Turbulence and Combustion* **104**, 579 (2020).
- [7] T. Kirchdoerfer and M. Ortiz, Data-driven computational mechanics, *Computer Methods in Applied Mechanics and Engineering* **304**, 81 (2016).
- [8] F. E. Bock, R. C. Aydin, C. J. Cyron, N. Huber, S. R. Kalidindi, and B. Klusemann, A review of the application of machine learning and data mining approaches in continuum materials mechanics, *Frontiers in Materials* **6**, 110 (2019).
- [9] J. Han, C. Ma, Z. Ma, and W. E, Uniformly accurate machine learning-based hydrodynamic models for kinetic equations, *Proceedings of the National Academy of Sciences* **116**, 21983 (2019).
- [10] D. Z. Huang, K. Xu, C. Farhat, and E. Darve, Learning constitutive relations from indirect observations using deep neural networks, *Journal of Computational Physics* , 109491 (2020).
- [11] K. Xu, D. Z. Huang, and E. Darve, Learning constitutive relations using symmetric positive definite neural networks, *Journal of Computational Physics* **428**, 110072 (2021).
- [12] F. Masi, I. Stefanou, P. Vannucci, and V. Maffi-Berthier, Thermodynamics-based artificial neural networks for constitutive modeling, *Journal of the Mechanics and Physics of Solids* **147**, 104277 (2021).
- [13] J. Han, L. Zhang, and W. E, Machine-learning-assisted modeling, *Physics Today* **74**, 36 (2021).
- [14] J.-L. Wu, R. Sun, S. Laizet, and H. Xiao, Representation of stress tensor perturbations with application in machine-learning-assisted turbulence modeling, *Computer Methods in Applied Mechanics and Engineering* **346**, 707 (2019).
- [15] M. I. Zafar, H. Xiao, M. M. Choudhari, F. Li, C.-L. Chang, P. Paredes, and B. Venkatachari, Convolutional neural network for transition modeling based on linear stability theory, *Physical Review Fluids* **5**, 113903 (2020).
- [16] S. Taghizadeh, F. D. Witherden, and S. S. Girimaji, Turbulence closure modeling with data-driven techniques: physical compatibility and consistency considerations, *New Journal of Physics* **22**, 093023 (2020).
- [17] R. Wang, R. Walters, and R. Yu, Incorporating symmetry into deep dynamics models for improved generalization, in *International Conference on Learning Representations* (2021).
- [18] S. B. Pope, A more general effective-viscosity hypothesis, *Journal of Fluid Mechanics* **72**, 331 (1975).
- [19] T. Gatski and C. Speziale, On explicit algebraic stress models for complex turbulent flows, *Journal of Fluid Mechanics* **254**, 59 (1993).
- [20] C. G. Speziale, S. Sarkar, and T. B. Gatski, Modelling the pressure-strain correlation of turbulence: an invariant dynamical systems approach, *Journal of Fluid Mechanics* **227**, 245 (1991).
- [21] T. B. Gatski, M. Y. Hussaini, and J. L. Lumley, *Simulation and modeling of turbulent flows* (Oxford University Press, 1996) Chap. 1.

- [22] L. Gao, Y. Du, H. Li, and G. Lin, Roteqnet: Rotation-equivariant network for fluid systems with symmetric high-order tensors, arXiv preprint arXiv:2005.04286 (2020).
- [23] Z. Long, Y. Lu, X. Ma, and B. Dong, PDE-Net: Learning PDEs from data, in *International Conference on Machine Learning* (PMLR, 2018) pp. 3208–3216.
- [24] L. Sun, H. Gao, S. Pan, and J.-X. Wang, Surrogate modeling for fluid flows based on physics-constrained deep learning without simulation data, *Computer Methods in Applied Mechanics and Engineering* **361**, 112732 (2020).
- [25] B. Kim, V. C. Azevedo, N. Thuerey, T. Kim, M. Gross, and B. Solenthaler, DeepFluids: A generative network for parameterized fluid simulations, *Computer Graphics Forum (Proc. Eurographics)* **38** (2019).
- [26] L. Lu, P. Jin, G. Pang, Z. Zhang, and G. E. Karniadakis, Learning nonlinear operators via deepnet based on the universal approximation theorem of operators, *Nature Machine Intelligence* **3**, 218 (2021).
- [27] C. Ma, B. Zhu, X.-Q. Xu, and W. Wang, Machine learning surrogate models for Landau fluid closure, *Physics of Plasmas* **27**, 042502 (2020).
- [28] M. D. Ribeiro, A. Rehman, S. Ahmed, and A. Dengel, DeepCFD: Efficient steady-state laminar flow approximation with deep convolutional neural networks, arXiv preprint arXiv:2004.08826 (2020).
- [29] Z. Li, N. Kovachki, K. Azizzadenesheli, B. Liu, K. Bhattacharya, A. Stuart, and A. Anandkumar, Neural operator: Graph kernel network for partial differential equations, arXiv preprint arXiv:2003.03485 (2020).
- [30] Z. Li, N. B. Kovachki, K. Azizzadenesheli, B. liu, K. Bhattacharya, A. Stuart, and A. Anandkumar, Fourier neural operator for parametric partial differential equations, in *International Conference on Learning Representations* (2021).
- [31] J. Han, L. Zhang, R. Car, and W. E, Deep Potential: a general representation of a many-body potential energy surface, *Communications in Computational Physics* **23**, 629 (2018).
- [32] L. Zhang, J. Han, H. Wang, W. Saidi, R. Car, and W. E, End-to-end symmetry preserving inter-atomic potential energy model for finite and extended systems, in *Advances in neural information processing systems* (2018) pp. 4436–4446.
- [33] X.-H. Zhou, J. Han, and H. Xiao, Frame-independent vector-cloud neural network for nonlocal constitutive modeling on arbitrary grids, *Computer Methods in Applied Mechanics and Engineering* **388**, 114211 (2022).
- [34] G. M. Sommers, M. F. C. Andrade, L. Zhang, H. Wang, and R. Car, Raman spectrum and polarizability of liquid water from deep neural networks, *Physical Chemistry Chemical Physics* **22**, 10592 (2020).
- [35] B. Eisfeld, Reynolds stress modeling for complex aerodynamic flows, in *Proceedings of the 5th European Conference on Computational Fluid Dynamics, ECCOMAS CFD*, edited by J. Pereira, A. Sequeira, and J. Pereira (2010).
- [36] R.-D. Cécora, R. Radespiel, B. Eisfeld, and A. Probst, Differential Reynolds-stress modeling for aeronautics, *AIAA Journal* **53**, 739 (2015).
- [37] B. Eisfeld, C. L. Rumsey, V. Togiti, S. Braun, and A. Stürmer, Reynolds-stress model computations of NASA juncture flow experiment, *AIAA Journal* , 1 (2021).
- [38] J. Slotnick, A. Khodadoust, J. Alonso, D. Darmofal, W. Gropp, E. Lurie, and D. Mavriplis, *CFD vision 2030 study: a path to revolutionary computational aerospace*, Tech. Rep. (National Aeronautics and Space Administration, Langley Research Center, Hampton, Virginia 23681-2199, 2014).
- [39] B. Launder, G. J. Reece, and W. Rodi, Progress in the development of a Reynolds-stress turbulence closure, *Journal of Fluid Mechanics* **68**, 537 (1975).
- [40] S. B. Pope, *Turbulent Flows* (Cambridge University Press, Cambridge, 2000).
- [41] B. Launder and B. Sharma, Application of the energy-dissipation model of turbulence to the calculation of flow near a spinning disc, *Letters in heat and mass transfer* **1**, 131 (1974).
- [42] P. R. Spalart and S. R. Allmaras, A one equation turbulence model for aerodynamic flows., *AIAA journal* **94** (1992).
- [43] G. Iaccarino, A. A. Mishra, and S. Ghili, Eigenspace perturbations for uncertainty estimation of single-point turbulence closures, *Physical Review Fluids* **2**, 024605 (2017).

- [44] K. Duraisamy, Z. J. Zhang, and A. P. Singh, New approaches in turbulence and transition modeling using data-driven techniques, in *53rd AIAA Aerospace Sciences Meeting* (2015) p. 1284.
- [45] H. Xiao, J.-L. Wu, S. Laizet, and L. Duan, Flows over periodic hills of parameterized geometries: A dataset for data-driven turbulence modeling from direct simulations, *Computers & Fluids* **200**, 104431 (2020).
- [46] H. Xiao and P. Jenny, A consistent dual-mesh framework for hybrid LES/RANS modeling, *Journal of Computational Physics* **231**, 1848 (2012).
- [47] The OpenFOAM Foundation, *OpenFOAM User Guide* (2020).
- [48] R. I. Issa, Solution of the implicitly discretised fluid flow equations by operator-splitting, *Journal of Computational Physics* **62**, 40 (1986).
- [49] X.-H. Zhou, J. Han, and H. Xiao, Learning nonlocal constitutive models with neural networks, *Computer Methods in Applied Mechanics and Engineering* **384**, 113927 (2021).
- [50] A. Paszke, S. Gross, F. Massa, A. Lerer, J. Bradbury, G. Chanan, T. Killeen, Z. Lin, N. Gimelshein, L. Antiga, *et al.*, Pytorch: An imperative style, high-performance deep learning library, in *Advances in neural information processing systems* (2019) pp. 8026–8037.
- [51] X.-H. Zhou, J. Han, and H. Xiao, Vector-cloud neural network with equivariance (VCNN-e) for tensors, <https://github.com/xuhuizhou-vt/VCNN-nonlocal-constitutive-model/tree/master/tensor-transport>.
- [52] J. L. Lumley and G. R. Newman, The return to isotropy of homogeneous turbulence, *Journal of Fluid Mechanics* **82**, 161 (1977).
- [53] P. S. Klebanoff, *Characteristics of turbulence in a boundary layer with zero pressure gradient*, Tech. Rep. (National Bureau of Standards, Gaithersburg, MD, 1955).